

Quantum Simulation of Ligand-like Molecules through Sample-based Quantum Diagonalization in Density Matrix Embedding Framework

Ashish Kumar Patra¹, Anurag K. S. V.¹, Sai Shankar P.¹, Ruchika Bhat^{1, 2}, Raghavendra V.³, Rahul Maitra⁴, and Jaiganesh G.*^{, 1}

¹Qclairvoyance Quantum Labs, Secunderabad, TG 500094, India.

²The University of Arizona, Tucson, AZ 85721, USA.

³SRM Institute of Science and Technology, Chennai, TN 603203, India.

⁴Indian Institute of Technology Bombay, Mumbai, MH 400076, India.

ABSTRACT

The accurate treatment of electron correlation in extended molecular systems remains computationally challenging using classical electronic structure methods. Hybrid quantum-classical algorithms offer a potential route to overcome these limitations; however, their practical deployment on existing quantum computers requires strategies that both reduce problem size and mitigate hardware noise. In this work, we combine Density Matrix Embedding Theory (DMET) with Sample-based Quantum Diagonalization (SQD) to compute ground-state energies of a set of natural ligand-like molecules in the minimal Slater Type Orbital (STO-3G) basis set. DMET provides a systematic fragmentation of a molecule into embedded impurity subproblems, while SQD enables construction and classical diagonalization of reduced configuration spaces through quantum sampling enhanced by iterative configuration recovery. The resulting embedded Hamiltonians are solved on IBM's Eagle R3 superconducting quantum hardware (IBM Sherbrooke). The DMET-SQD energies obtained for all systems considered exhibit strong agreement with DMET-FCI benchmark values within chemical accuracy (1 kcal/mol). These results demonstrate that sample-based quantum methods, when integrated with a robust embedding framework, can reliably extend quantum computation towards simulation of chemically relevant molecular systems, showcasing potential applications in the field of drug discovery.

Keywords: Quantum Computing · Quantum Simulation · Quantum Chemistry · Sample-based Algorithms · Embedding Methods · Hybrid Quantum-Classical Algorithms

1 Introduction

In quantum chemistry, the accurate simulation of many-electron systems remains a central goal. However, the increasing complexity of molecular systems renders such endeavours computationally demanding, often necessitating varying levels of approximation¹. Current classical computational resources are insufficient to fully capture electron correlation in larger molecular systems, such as proteins. More recently, distributed computing and an efficient flavor of Full Configuration Interaction (FCI) known as the Small-Tensor Product Distributed Active Space (STP-DAS) has been used to simulate the *HBrTe* molecule leading to the diagonalization of a Hilbert space exceeding 10^{15} determinants² involving 88 electrons and 100 spin orbitals in the x2c-TZVPall basis set³. For comparison, one of the largest conventional FCI simulations carried out using classical methods involved propane (C_3H_8), requiring the diagonalization of a Hilbert space spanning approximately 1.31×10^{12} determinants⁴, even when employing a minimal STO-3G basis set⁵. In quantum chemistry, Hartree-Fock (HF) theory continues to serve as the foundational approximation for all subsequent methods⁶.

With the advent of quantum computers, the accurate simulation of chemically and biologically relevant systems are expected to become increasingly tractable. Quantum algorithms promise the capability to model and evaluate protein-ligand interactions⁷⁻⁹ and binding energetics, explore conformational landscapes of flexible bio-molecules¹⁰⁻¹⁶-tasks that rapidly become intractable on classical computers¹⁷. This has motivated increasing interest in quantum computing, which offers alternative algorithmic frameworks capable of addressing many-electron correlations more efficiently^{18, 19}.

Fault-tolerant Application-Scale Quantum (FASQ)²⁰ algorithms, such as Quantum Phase Estimation (QPE)²¹ and Quantum Singular Value Transformation (QSVT)^{22, 23}, face significant challenges due to their requirement for deep quantum circuits,

*(Corresponding Author) email: jaiganesh@qclairvoyance.in, drjaiganesh15@gmail.com

which remain impractical on current Noisy Intermediate-Scale Quantum (NISQ) hardware²⁴. To facilitate execution on near-term devices, variational approaches such as the Variational Quantum Eigensolver (VQE)²⁵ were proposed. VQE evaluates the expectation value of the Hamiltonian directly through a hybrid classical-quantum optimization loop, iteratively improving the overlap between the parametrized quantum state and the true ground state. Recent developments²⁶ have produced more hardware-efficient variants, yet key limitations persist, including statistical fluctuations and physical noise inherent to NISQ devices, as well as the requirement for prohibitively large numbers of samples and extensive error mitigation strategies²⁷.

Early hardware demonstrations of molecular problems using VQE, such as protein-ligand interactions, have been limited to active spaces involving around four qubits⁷, primarily restricted to small organic systems. To overcome these limitations, sample-based approaches such as Sample-Based Quantum Diagonalization (SQD)²⁸ have emerged. SQD integrates Quantum Selected Configuration Interaction (QSCI)²⁹ with an error-mitigation scheme known as Iterative Self-Consistent Configuration Recovery (S-CoRe)²⁸ and employs classical Selected Configuration Interaction (SCI)³⁰ for post-processing diagonalization. These methods have enabled the quantum sampling of molecules with up to 36 spatial orbitals, including the [4Fe-4S] complex in a 77-qubit experiment, using 6400 nodes of the *Fugaku* super-computer²⁸.

While quantum computers are anticipated to handle strongly correlated systems more effectively—providing a compelling rationale for their adoption, counterarguments emphasize potential limitations³¹. Nonetheless, within the emerging paradigm of Quantum-Centric Super-Computing (QCSC)²⁸, where classical supercomputers are coupled with quantum computers in a hybrid framework, SQD has facilitated a series of further algorithmic advancements.

Recent developments in sample-based quantum algorithms include applications to materials simulation³², excited-state energy estimation³³, hybrid methods combining SQD with Krylov Subspace Diagonalization³⁴ and QDrift³⁵, leading to techniques such as Sample-based Krylov Quantum Diagonalization(SKQD)³⁶, Quantum Krylov using Unitary Decomposition(QKUD)³⁷ and SqDRIFT³⁸. Additionally, methods like Handover Iterative VQE (HI-VQE)³⁹ have been developed to iteratively expand the configuration space, achieving chemical accuracy while sampling only a fraction of the symmetry space⁴⁰, that is, configurations obeying number and spin symmetries.

Classical fragmentation techniques offer a practical route to handling the exponential scaling of electronic structure methods by dividing large molecular systems into smaller subsystems. This fragment-based viewpoint allows chemically realistic systems to be studied without treating the entire system at once, while still retaining a meaningful description of inter-fragment interactions. By decomposing the global wavefunction or Hamiltonian into fragment-level contributions, these approaches enable the treatment of chemically realistic systems while retaining a controlled description of inter-fragment interactions. Prominent examples include Density Matrix Embedding Theory (DMET)^{41–44} and its multi-reference variants^{45,46}, Divide and Conquer (DC) method^{47,48}, and the Fragment Molecular Orbital (FMO) framework⁴⁹, all of which have demonstrated practical applicability across a wide range of molecular and materials problems⁵⁰. These techniques provide a systematic route for reducing the effective dimensionality of quantum chemical calculations by localizing electronic structure in real space or orbital subspaces, while incorporating environmental effects through embedding potentials, density constraints, or effective Hamiltonians.

Beyond these foundational approaches, several modern fragmentation schemes aim to preserve higher-order correlation effects while maintaining computational efficiency^{51–57}. Coupled-cluster downfolding methods construct effective low-dimensional Hamiltonians by integrating out inactive degrees of freedom using classical CC theory, yielding size-consistent and systematically improvable reduced models^{51,52,58}. Variational Localized Active Space methods, such as LASSCF^{53,54}, explicitly partition the active space into weakly entangled local subspaces that can be optimized independently, providing a natural interface for hybrid classical-quantum workflows. Related embedding paradigms include wavefunction-based embedding methods (EWF)⁵⁵, Many-Body Expansion (MBE)^{56,57}, and Dynamical Mean-Field Theory (DMFT)^{59,60}, which employ different strategies for capturing non-local correlation and dynamical effects. More recently, Bootstrap Embedding (BE)⁶¹ has been introduced as a hybrid quantum-classical embedding framework that employs a self-consistent feedback loop between quantum impurity solvers and an effective classical environment.

In parallel, several approaches have focused on adapting classical fragmentation techniques for use with quantum simulation algorithms. Notable examples include DMET-VQE implementations on superconducting and trapped-ion platforms^{7,62}, as well as DMET-SQD¹⁴ and EWF-SQD⁶³ approaches demonstrated on IBM quantum hardware. Related efforts such as divide-and-conquer VQE (DC-VQE)⁶⁴ and fragment molecular orbital extensions to quantum solvers, including Effective FMO-VQE⁶⁵, further illustrate the breadth of strategies combining classical fragmentation with quantum sampling or variational techniques. Collectively, these works define a growing ecosystem of hybrid methods that aim to balance accuracy, scalability, and near-term hardware constraints in quantum-enabled electronic structure calculations.

SQD has gained significant interest in recent times^{28,39,40,66} and is subject to further exploration to develop and assess its performance within fragmentation frameworks^{14,63,67}. Towards this, we develop the sample-based technique, SQD within the DMET framework and systematically study its ability in accurate prediction of ground-state energetics across a series of ligand-like molecules. These ligand-like molecules exhibit reduced symmetry in contrast to the highly symmetric model systems

considered in previous studies¹⁴. As a result, electron delocalization over the entire molecule introduces qualitatively different challenges for embedding and sampling, providing a rigorous test of the robustness and practical applicability of the proposed approach. The ligand-like molecules considered for the study include: Cyanic Acid(*HOCN*), Formaldehyde Oxime (*CH*₃*NO*), O-methyl-hydroxylamine (*CH*₅*NO*), Methyl Isocyanate (*C*₂*H*₃*NO*), Acetaldehyde Oxime (*C*₂*H*₅*NO*), Carbamide/Urea (*CH*₄*N*₂*O*), Nitrosyl Chloride (*NOCl*), and Hydroxythiocyanate (*HOSCN*). All of these compounds have molecular weights below 76 Da (see Fig. 4.1) and together span a chemically diverse set of small, pharmacologically motivated molecular systems. Several members of this set, particularly urea derivatives and methoxyamine-related systems have established relevance in medicinal chemistry^{68–71}. This makes the collection an appropriate testbed for assessing sample-based quantum simulation techniques in the context of drug-discovery-oriented molecular systems.

Concisely detailing the work, in **Section 2** an overview of the methods used are described briefly, in **Section 3** the experimental details and methodology are discussed, in **Section 4** the results obtained are discussed and finally in **Section 5** we conclude the work and mention future prospects.

2 Theoretical Background

2.1 Hamiltonian Formulation and Local Unitary Cluster Jastrow ansatz

Under the Born-Oppenheimer approximation⁷², the electronic structure problem is most conveniently expressed in second quantization, where the Hamiltonian is written in terms of fermionic creation and annihilation operators acting on a basis of spin orbitals⁷³. This representation separates one-electron and two-electron contributions and forms the natural interface for quantum simulation, since it can be systematically mapped onto qubit operators using standard fermion-to-qubit encodings such as the Jordan-Wigner transformation⁷⁴. In this work, we initialize the quantum register in the restricted Hartree-Fock (HF) reference state, which is a single Slater determinant that is straightforward to prepare on quantum hardware and typically exhibits a significant overlap with the true ground state:

$$\hat{H}_{sq} = \sum_{i,j} h_{ij} \hat{a}_i^\dagger \hat{a}_j + \frac{1}{2} \sum_{p,q,r,s} h_{pqrs} \hat{a}_p^\dagger \hat{a}_q^\dagger \hat{a}_r \hat{a}_s. \quad (1)$$

Starting from this reference, we construct a correlated variational wavefunction using the Local Unitary Cluster Jastrow (LUCJ) ansatz⁷⁵, which is designed to balance chemical expressivity with circuit efficiency on near-term quantum devices. The ansatz parameters are initialized using amplitudes inspired by coupled-cluster singles and doubles (CCSD) theory^{76,77}, providing a chemically motivated starting point for optimization. The LUCJ ansatz consists of multiple layers, each comprising an orbital-rotation operator, a diagonal Jastrow interaction that captures electron-electron correlations, and the inverse orbital rotation, thereby incorporating correlation effects in a structured and hardware-aware manner^{78,79}. The resulting variational state is given by

$$|\psi\rangle_{UCJ} = \prod_{\mu=1}^L e^{\hat{K}_\mu} e^{\hat{J}_\mu} e^{-\hat{K}_\mu} |\psi\rangle_{HF}. \quad (2)$$

Here, $|\psi\rangle_{HF}$ denotes the Hartree-Fock reference state and L is the total number of LUCJ layers. The operators \hat{K}_μ and \hat{J}_μ respectively generate orbital rotations and two-body correlation effects within each layer, enabling the ansatz to systematically incorporate electronic correlation beyond the mean-field level while maintaining a circuit structure amenable to near-term quantum hardware. For closed-shell systems, a spin-balanced form of the ansatz is employed to enforce spin symmetry and reduce the number of independent variational parameters, improving optimization stability without sacrificing expressivity.

2.2 Density Matrix Embedding Theory

Density Matrix Embedding Theory (DMET)⁴² is a frequency-independent quantum embedding method conceptually related to Dynamical Mean-Field Theory (DMFT)⁵⁹, in which the environment of a chosen fragment is represented through a set of entangled orbitals, referred to as bath orbitals. In DMET, a set of user-defined fragment orbitals A_y is selected from a localized orbital basis, and the remaining orbital space constitutes the environment Env_y . This environment is decomposed into entangled bath orbitals and unentangled core and virtual orbitals according to

$$Env_y = B_y \cup Cor_y \cup Vir_y, \quad (3)$$

where B_y denotes the bath orbitals capturing fragment-environment entanglement, while Cor_y and Vir_y correspond to unentangled occupied and virtual orbitals, respectively.

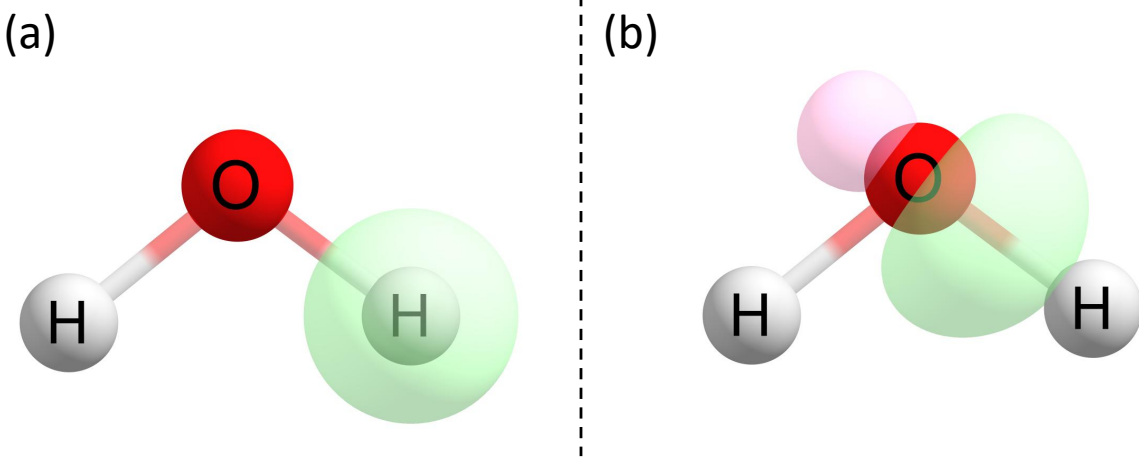


Figure 2.1. Illustrative example of bath-orbital construction for the H_2O molecule in the STO-3G basis. The system is fragmented so that the orbital localized on a single hydrogen atom constitutes the fragment. (a) shows an iso-surface of this fragment orbital; (b) shows the corresponding bath orbital obtained via DMET, which is a linear combination of the remaining localized spatial orbitals in the molecular orbital basis. Together, (a) and (b) span the impurity subspace for the H-fragment.

The bath orbitals are constructed from a mean-field reference (typically Hartree-Fock) by projecting the one-particle reduced density matrix (1-RDM) onto the fragment subspace and diagonalizing the resulting matrix. The eigenvectors with fractional occupations define the bath orbitals, and their number is bounded by the number of fragment orbitals^{80,81}. An illustrative example of bath construction for a hydrogen fragment in a water molecule is shown in Fig. 2.1. The fragment and bath orbitals together form the impurity space on which an embedded Hamiltonian is solved to obtain the correlated wavefunction. A global chemical potential μ_{glob} is adjusted to ensure electron number consistency across all fragments, corresponding to a one-shot interacting bath formulation⁴¹.

The fragment energy E_{A_y} is given by

$$E_{A_y} \approx \sum_{p \in A_y} \left(\sum_q^{L_{A_y} + L_{B_y}} \left(\frac{t_{pq} + \bar{h}_{pq}^y}{2} \right) D_{qp}^y + \frac{1}{2} \sum_{qrs}^{L_{A_y} + L_{B_y}} (pq|rs) P_{qp|sr}^y \right), \quad (4)$$

where E_{A_y} denotes the energy contribution associated with fragment A_y . The indices p, q, r, s label spatial orbitals belonging to the impurity space, defined as the union of fragment and bath orbitals with total dimension $L_{A_y} + L_{B_y}$. The matrix elements t_{pq} denote the one-electron integrals in the molecular orbital basis, while \bar{h}_{pq}^y are effective one-body terms incorporating the mean-field contribution of the core orbitals. The quantities $D_{qp}^y = \langle \hat{a}_p^\dagger \hat{a}_q \rangle$ and $P_{qp|sr}^y = \langle \hat{a}_p^\dagger \hat{a}_r^\dagger \hat{a}_s \hat{a}_q \rangle$ denote the fragment one- and two-particle reduced density matrices (1-RDM and 2-RDM), respectively. The two-electron integrals $(pq|rs)$ are Coulomb integrals in the molecular orbital basis. The prefactors of 1/2 avoid double counting when summing over all orbital indices, and the total energy of the system is obtained by summing the contributions from all fragments.

2.3 Sample-based Quantum Diagonalization

SQD²⁸ is a combination of the quantum sampling method QSCI²⁹ and an error-mitigation technique introduced in the work, S-CoRe, which “recovers” the noisy configurations. These configurations thus obtained create a sub-space, which is further expanded, and then the projection sub-space is obtained over which SCI³⁰ is performed to obtain the ground state energy.

2.3.1 Quantum State Preparation and Sampling

We begin with the goal of approximation of the ground state energy of a many-body Hamiltonian by constructing and (classically) diagonalizing a reduced Hilbert space that contains the *dominant configurations* contributing to the ground state configuration, *sampled using a quantum computer*. Starting from an approximate ground state, like $|\psi\rangle_{HF}$, a variational ansatz is initialized with suitable parameters: $|\psi\rangle_{init} = \hat{U}(\theta_1, \theta_2, \dots, \theta_n) |\psi\rangle_{HF}$ (in our case, the LUCJ ansatz with CCSD parameters) to increase the overlap between the trial state with the true ground state, as provided in Fig. 2.2.

Quantum sampling is performed in the computational basis, and a set $\mathcal{S}_{\text{samp}}$ is obtained with d configurations:

$$\mathcal{S}_{\text{samp}} = \{|\phi_1\rangle, |\phi_2\rangle, \dots, |\phi_d\rangle\} \quad (5)$$

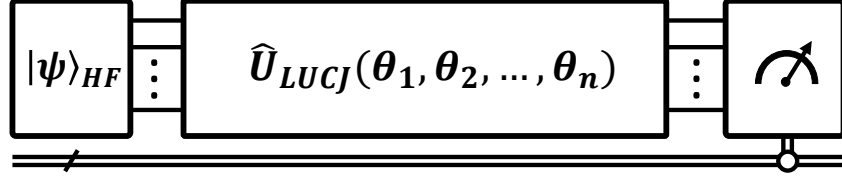


Figure 2.2. Quantum Circuit Diagram for performing Sample-based Quantum Diagonalization. The initial state is prepared as the Hartree-Fock configuration, and is acted upon by an LUCJ ansatz which is pre-initialized with t_i^a and t_{ij}^{ab} parameters obtained through CCSD calculation. Finally, measurement is performed in the $\hat{\sigma}_z$ basis.

where every $|\phi_i\rangle$ can be represented as a tensor product of the α spin and β spin configurations: $|\phi_i\rangle = |\alpha_i\rangle \otimes |\beta_i\rangle$. The total number of electrons in the molecular systems is designated as N_{elec} , and correspondingly the number of electrons in α configuration and β configurations are designated as N_α and N_β respectively. For molecular systems which contain fully-filled spatial orbitals (closed-shell) and which possess zero spin, the following conditions must be satisfied for all the computational basis states contributing to the eigen-states of the system:

$$N_\alpha + N_\beta = N_{elec}; \quad N_\alpha - N_\beta = 0. \quad (6)$$

Due to the noisy nature of quantum computers, we end up also sampling configurations which violate the particle-number and spin- z symmetries mentioned in Eq.(6). These “noisy” configurations are recovered using configuration recovery²⁸.

2.3.2 Self-Consistent Iterative Configuration Recovery

S-CoRe, or Configuration Recovery, is an iterative procedure designed to restore the sampled noisy configurations. Given an approximate ground-state occupation number distribution for the state-vector $|\Psi\rangle$:

$$n_{p\sigma} = \langle \Psi | \hat{a}_{p\sigma}^\dagger \hat{a}_{p\sigma} | \Psi \rangle, \quad (7)$$

where $n_{p\sigma}$ is the occupancy corresponding to the p^{th} spatial orbital with σ spin configuration, S-CoRe updates each sampled configuration, over multiple batches (number of batches is denoted by K) by probabilistically flipping occupations of the spin-orbitals based on the values of $n_{p\sigma}$ until the total electron number and spin projection match the target values. This produces a set of corrected configuration sub-spaces $\mathcal{S}_{CR}^{(b)}, \forall b \in K$ that respect the intended symmetries while remaining close to the original sampled distribution.

For projection and diagonalization, the sub-spaces $\mathcal{S}_{CR}^{(b)}$ are converted to $\mathcal{S}_{proj}^{(b)}$ as detailed in Sec. 2.3.3. With the $E^{(b)}$ and $|\Psi^{(b)}\rangle$ obtained post the classical diagonalization for all the K batches, the lowest energy $\min_b E^{(b)}$ is taken as the current best estimate, and the average orbital occupation is thus calculated as:

$$n_{p\sigma} = \frac{1}{K} \sum_{b=1}^K \langle \Psi^{(b)} | \hat{a}_{p\sigma}^\dagger \hat{a}_{p\sigma} | \Psi^{(b)} \rangle, \quad (8)$$

which is again used in the next iteration and so on. This self-consistent iteration ensures that the symmetry constraints are enforced, and the recovered sub-space contains configurations closer to the desired orbital occupation distribution. From these recovered configurations at each iteration, K batches of subspaces $\{\mathcal{S}_{CR}^{(b)}\}_{b \in K}$ are obtained.

2.3.3 Selected Configuration Interaction

For the set of configurations obtained in the b^{th} batch, the sub-space is designated as $\mathcal{S}_{CR}^{(b)}$. As the subsequent steps remain the same for all the batches, we shall drop the super-script and denote the sub-space as \mathcal{S}_{CR} without loss of generality.

In SQD, the configurations $\mathcal{S}_{CR} = \{|\alpha_1\rangle \otimes |\beta_1\rangle, |\alpha_2\rangle \otimes |\beta_2\rangle, \dots, |\alpha_d\rangle \otimes |\beta_d\rangle\}$ do not represent the sub-space onto which the Hamiltonian is projected. Instead in the case of **closed-shell systems** all the unique alpha configurations $\mathcal{A}_{unique} = \{|\alpha_1\rangle, |\alpha_2\rangle, \dots, |\alpha_d\rangle\}$ and unique beta configurations $\mathcal{B}_{unique} = \{|\beta_1\rangle, |\beta_2\rangle, \dots, |\beta_d\rangle\}$ are again made into a final set:

$$\mathcal{P}_{unique} = \mathcal{A}_{unique} \cup \mathcal{B}_{unique} \quad (9)$$

Now, a new configuration space is obtained from the tensor product of \mathcal{P}_{unique} with itself, which we define as \mathcal{S}_{proj} :

$$\mathcal{P}_{unique} \otimes \mathcal{P}_{unique} = \mathcal{S}_{proj} = \{|\lambda\rangle \otimes |\phi\rangle : \forall |\lambda\rangle \in \mathcal{P}_{unique}, \forall |\phi\rangle \in \mathcal{P}_{unique}\}. \quad (10)$$

Hence, \mathcal{S}_{proj} is the **sub-space onto which the Hamiltonian is projected onto, and not the \mathcal{S}_{CR} obtained after configuration recovery**. \mathcal{S}_{proj} is subsequently diagonalized using Davidson's Algorithm⁸². The construction in which the unique configurations from \mathcal{A}_{unique} and \mathcal{B}_{unique} are merged into \mathcal{P}_{unique} , followed by forming the tensor-product space $\mathcal{P}_{unique} \otimes \mathcal{P}_{unique}$, is motivated by the observation that the ground-state wavefunction usually exhibits correlated contributions from configuration pairs. In particular, if a configuration of the form $|\alpha\rangle \otimes |\beta\rangle$ carries a non-zero amplitude in the ground state, then it is typically the case that the corresponding configuration $|\beta\rangle \otimes |\alpha\rangle$ also contributes with comparable weight³⁹.

The Hamiltonian is projected (for every b^{th} sub-space) into the sub-space \mathcal{S}_{proj} ,

$$\hat{H}_{\mathcal{S}_{proj}} = \hat{P}_{\mathcal{S}_{proj}} \hat{H} \hat{P}_{\mathcal{S}_{proj}}, \quad \hat{P}_{\mathcal{S}_{proj}} = \sum_{\mathbf{x} \in \mathcal{S}_{proj}} |\mathbf{x}\rangle \langle \mathbf{x}|, \quad (11)$$

and the solution is obtained by performing diagonalization using Davidson's method⁸², finally providing us $E^{(b)}$ and $|\Psi^{(b)}\rangle$, which are again utilized in Eq. (8) to obtain the average orbital occupancies.

Because the diagonalization cost scales polynomially in $|\mathcal{S}_{proj}|$, the method remains tractable as long as the number of selected configurations does not grow exponentially with system size⁸².

3 Methodology

This section describes the DMET-SQD framework, integrating fragmentation, impurity solving, and self-consistent quantum procedures via global chemical potential. Sec. 3.1 details the workflow; Sec. 3.2 covers hardware, software, and settings.

3.1 DMET-SQD Workflow

The workflow¹⁵ used to perform DMET-SQD is as follows:

1. The molecular co-efficient matrix C , and the HF determinant (in the case of single-reference systems) of the whole system are obtained using Restricted HF method (here we only encounter molecular systems with fully filled spatial orbitals).
2. Then, the molecular spatial orbitals are localized (using Meta-Löwdin localization⁸³) and based on the user-defined criteria (in this case, one atom per fragment), the orbitals are fragmented.
3. The bath orbitals are constructed with the remaining environment orbitals for the fragment A_y . Here, the occupation threshold ε_{occ} is set to 10^{-13} for discarding virtual orbitals⁴¹.
4. The Fock matrix \hat{F}_{imp} (where $imp = A_y + B_y$) for each of the impurities is obtained, and the chemical potential μ_{glob} is subtracted from the diagonal entries corresponding to the fragment orbitals:

$$\hat{F}_{imp}^{new}(\mu_{glob}) = \hat{F}_{imp} - \mu_{glob} \hat{P}_{frag}, \quad \hat{P}_{frag} = \begin{cases} 1 & \text{if } i = j \text{ and } i \in A_y \\ 0 & \text{otherwise} \end{cases} \quad (12)$$

5. Using $\hat{F}_{imp}^{new}(\mu_{glob})$ from Eq. (12), an SCF calculation is carried out in the impurity space to obtain updated molecular properties, such as the impurity coefficient matrix $C_{imp}^{new}(\mu_{glob})$ and the corresponding one-particle density matrix $D^y(\mu_{glob})$. The standard convention is to initialize $\mu_{glob}^{init} = 0$.
6. Now, we use SQD, *as the high-level solver* to estimate the ground state energy and eigen-vector of these "impurities". The one-electron ($h_{imp}^{pq}(\mu_{glob})$) and two-electron ($h_{imp}^{pqrs}(\mu_{glob})$) Hamiltonian terms (where $pqrs \in imp$) obtained after the localization, serve as the $\hat{H}_{emb}(\mu_{glob})$, and the configurations obtained through quantum sampling (and subsequent Configuration Recovery) are used to form the subspace onto which \hat{H}_{emb} is projected. *In the case of calculating the reference energies, this step would be replaced by FCI, without any loss of generalization.*
7. Using the eigen-vector obtained in the previous step, the following quantities are calculated:

- fragment energy $E_{A_y}(\mu_{glob})$ using Eq. (4),
- number of electrons in the fragment¹⁵ $N_{A_y}^{ele}$, where $N_{A_y}^{ele}(\mu_{glob}) = \sum_{p \in A_y} D_{pp}^y(\mu_{glob})$
- 1-RDM $D_{pq}^y(\mu_{glob})$ and
- 2-RDM $P_{qp|sr}^y(\mu_{glob})$ of the impurities, where $pqrs \in imp$.

8. Now similar to the fragment A_y , the steps 2 to 6 are repeated for all the remaining $N_{frag} - 1$ fragments, where N_{frag} represents the number of fragments in the system. The total energy $E_{tot}(\mu_{glob})$, the number of electrons of the system N_{tot} , and the error in electron number N_{err}^{ele} can be thus obtained by:

$$E_{tot}(\mu_{glob}) = E_{nuc} + \sum_y^{N_{frag}} E_{A_y}(\mu_{glob}), \quad N_{tot}(\mu_{glob}) = \sum_y^{N_{frag}} N_{A_y}^{ele}(\mu_{glob}), \quad N_{err}^{ele}(\mu_{glob}) = N_{tot}(\mu_{glob}) - N_{true} \quad (13)$$

where E_{nuc} is the nuclear repulsion energy of the total system, and N_{true} is the exact number of electrons in the system (which we know a priori).

9. Next, the root of the function $N_{err}^{ele}(\mu_{glob})$ is computed to within the convergence threshold ϵ_{conv} , by iteratively updating μ_{glob} , and repeating the steps 2 to 7, using a root finding method (in this case we use Newton-Secant method⁸⁴). In other words, we wish to obtain a μ_{glob}^* such that:

$$|N_{tot}(\mu_{glob}^*) - N_{true}| < \epsilon_{conv}. \quad (14)$$

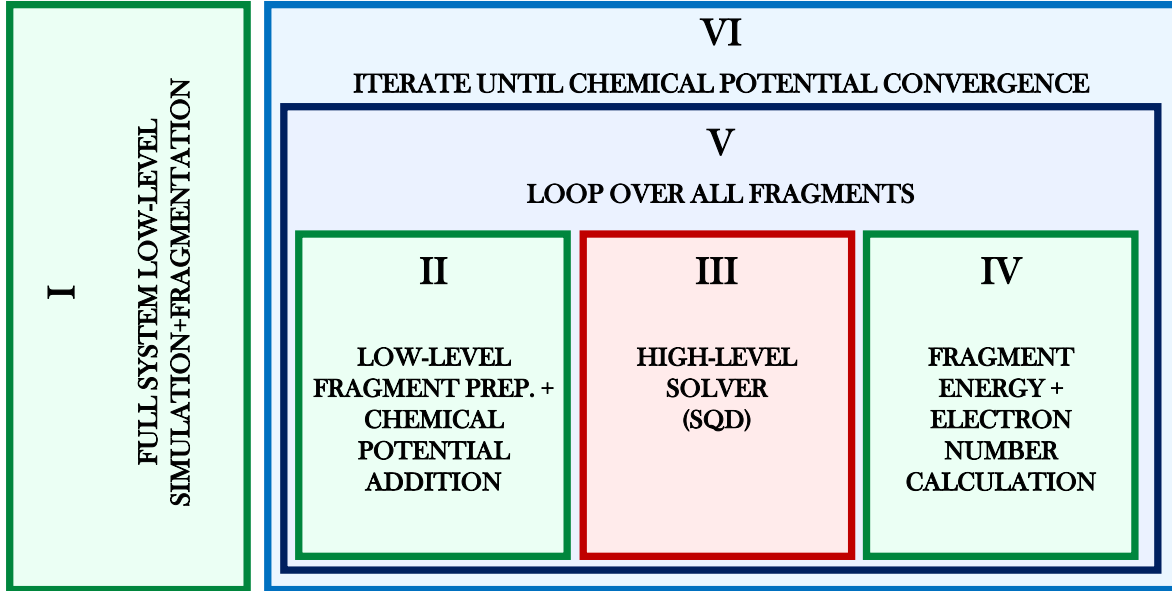


Figure 3.1. A simplified workflow for DMET-SQD

The above given workflow can be segmented out into six major sections, in the following manner: **Step 1**, **Step 2** can be considered to fall under a common section, designated as **Part I**, which deals with initial low-level solving of the entire system to obtain certain pre-requisites, **Steps 3, 4 and 5**, deal with the creation of bath orbitals, and the inclusion of μ_{glob} into the hamiltonians of the impurities, which can be designated as **Part II**. **Step 6** falls under **Part III**, where the previously obtained Hamiltonians are solved using a high-level solver, such as SQD. **Step 7** involves obtaining the relevant information from the state-vector obtained from high-level solving. This crucial step allows us to perform further iterations, and can be designated as **Part IV**. **Step 8** and **Step 9** involve looping over the fragments to obtain the total energy and the number of electrons in the system, and subsequently tweaking μ_{glob} to satisfy Eq. (14), respectively. These steps are designated as **Part V** and **Part VI**. A diagrammatic workflow with the above-mentioned parts is provided in Fig. 3.1.

3.2 Experimental Details

The sampling part of the quantum simulation experiments in this work was executed on the Eagle R3 quantum processor (IBM Sherbrooke, containing 127 qubits)⁷⁹. The corresponding hardware calibration metrics recorded immediately prior to the computation are provided in Sec. C. These values represent the initial calibration state of the device and should not be interpreted as a faithful reflection of the noise characteristics during execution. This distinction is important, as the full set

of molecular simulations required approximately two days to complete, largely due to queueing delays between successive quantum-sampling jobs, *during which hardware performance may drift*.

For DMET-SQD and DMET-FCI, `Tangelo` v0.4.3⁸⁵ was used. LUCJ circuits were generated using `ffsim` v0.10.0⁸⁶, and quantum circuits were constructed and transpiled with `Qiskit` v1.4.2⁸⁷ and `Qiskit IBM Runtime` v0.36.1. All quantum-chemistry tasks (HF, CCSD, and SCI) were carried out using `PySCF` v2.10.0⁸³. The root-finding method used was the Newton–Secant method from `scipy` v1.15.3⁸⁸.

The molecules taken for the study are shown in Sec. B. The STO–3G basis set was employed in this work, due to its minimal size and computational efficiency, which make it particularly well suited for quantum simulations on current NISQ-era hardware, and the fragmentation was performed such that each atom in the fragment is treated as a fragment for all the molecules.

While ROHF-based DMET formulations for open-shell systems are well-established^{89–91}, the ligand-like molecules considered in this study are closed-shell systems, and a restricted Hartree-Fock reference is therefore employed for constructing the DMET bath. The fragmentation scheme adopted is one-atom-per-fragment as a stringent test of bath orbital construction, including chemically nontrivial cases where covalent bonds, such as double bonds, are cut across fragments. This aggressive partitioning allows us to assess whether the resulting loss in correlation is captured consistently by both DMET-SQD and the reference DMET-FCI calculations within chemical accuracy, while simultaneously keeping the sample space as small as possible to reduce shot budget for SQD sampling and also to reduce the classical post-processing overhead.

Since the SQD solver relies on SCI for diagonalization, it is formally neither size-consistent nor size-extensive, and its accuracy depends explicitly on the configurations retained. However, the hardware-driven sampling and subsequent configuration recovery ensure that the most dominant determinants across the full Hilbert space are naturally picked, and this dominant subspace can be systematically enlarged to improve the accuracy. This ensures that despite the formal lack of size-consistency, the numerical accuracy is maintained even for larger basis sets and more extended systems within the scope of the approach considered here.

For this reason, FCI is employed as the benchmark solver, as it accesses the full configuration space and is both size-consistent and size-extensive. The minimal basis set and force-field-optimized geometries were chosen to enable a controlled methodological benchmarking of DMET-SQD against DMET-FCI under current NISQ-era hardware and access constraints, where qubit counts, circuit depths, and limited execution time make the use of larger basis sets impractical. This choice further allows FCI to be performed without active-space truncation, ensuring that any degradation in correlation arises from the embedding and solver strategy, and thereby validating the ability of DMET-SQD to reproduce the correlation capture of DMET-FCI within the bounds of the present study.

The number of shots used for quantum sampling was 10^4 and was kept consistent across all the impurities, regardless of the number of spin orbitals within them. For each impurity, 5 iterations of S-CoRe were performed. The maximum allowed samples per batch was set to 10^5 . The circuits were transpiled⁹² with optimization set to level 3, and no additional error handling techniques were employed in these series of experiments. The convergence threshold $\varepsilon_{\text{conv}}$ for μ_{glob} was set to 1.48×10^{-8} , which is the default parameter in `scipy.optimize.newton` method.

4 Results and Discussion

The absolute energy differences between the DMET-SQD energies and DMET-FCI energies of the molecules are presented in Fig. 4.1. As is evident, the energy differences obtained are consistently lower than 10^{-5} Ha, and in some cases are within micro-Hartree precision in comparison to DMET-FCI.

The details pertaining to the fragmentation settings, quantum resource requirements, and the dimensions of the symmetry space and Hilbert space are summarized in Table 4.1. The resource estimation is presented in the IBM Sherbrooke superconducting hardware basis gate set $\{X, R_z, \sqrt{X}(S_x), ECR\}$. The largest quantum-sampling experiment employed 30 qubits, with a symmetry-space dimension of 25,050,025 and a Hilbert-space dimension of 1,073,741,824. The largest quantum circuit depth was 1081. These entries have been highlighted in the table to indicate the maximal values observed in our study.

The simulation results showing the energies obtained through DMET-SQD on a quantum computer, DMET-FCI as reference, and the absolute energy difference between them are shown in Sec. B. The energy differences lie along the range of micro-Hartree, indicating strong agreement with the reference. The geometric co-ordinates of the molecules used for simulation were geometry-optimized (force-field level)⁹³ and are given in the Sec. A.

These results indicate that the quantum sampling, configuration recovery and subsequent creation of projection sub-space through symmetrized expansion of the unique spin configurations (Eq. 9 and Eq. 10), is leading to diagonalization over a sub-space which is a sizable fraction of the *symmetry space*³⁹.

Figure 4.2 illustrates the convergence behavior of the DMET-SQD workflow with respect to the number of iterations N_{it} (required for μ_{glob} convergence) for a set of ligand-like molecules. Panel (a) reports the absolute energy difference $\Delta E = |E_{\text{DMET-SQD}} - E_{\text{DMET-FCI}}|$ on a logarithmic scale, while panel (b) shows the corresponding electron number deviation N_e^{err} for each impurity. A systematic and monotonic reduction of errors is observed as the number of iterations increases,

Table 4.1. Quantum resource estimation summary for the molecular fragments. Beginning from the left: Chemical formula of the molecule, Fragment, number of spatial orbitals and number of electrons represented as (o, e), number of qubits used, depth of the quantum circuit, number of R_z , $\sqrt{X}(S_x)$, X , ECR gates used respectively for the specific instance of execution, dimension of the Symmetry Space(|S.SI|), dimension of the Hilbert Space(|H.SI|), the QPU time taken for performing DMET-SQD, and the number of iterations for μ_{glob} convergence (N_{it}).

Molecule	Frag	(o, e)	Qubits	Depth	R_z	S_x	X	ECR	S.SI	H.SI	T(s)	N_{it}
<i>HOCN</i>	[H]	(10, 10)	20	365	1833	1548	88	550	63,504	1,048,576	68	4
	[O]	(10, 10)	20	343	1804	1410	126	550	63,504	1,048,576		
	[C]	(10, 10)	20	389	1939	1524	108	584	63,504	1,048,576		
	[N]	(2, 2)	4	34	46	38	0	12	4	16		
<i>CH₃NO</i>	[C]	(10, 10)	20	366	1847	1454	134	580	63,504	1,048,576	107	4
	[H]	(2, 2)	4	34	43	38	0	12	4	16		
	[H]	(2, 2)	4	34	44	38	0	12	4	16		
	[H]	(2, 2)	4	35	47	38	0	12	4	16		
	[N]	(10, 10)	20	341	1814	1511	88	542	63,504	1,048,576		
	[O]	(10, 10)	20	378	1893	1479	138	586	63,504	1,048,576		
<i>CH₅NO</i>	[C]	(10, 10)	20	369	1946	1578	109	586	63,504	1,048,576	130	4
	[H]	(2, 2)	4	35	45	38	0	12	4	16		
	[H]	(2, 2)	4	35	48	38	0	12	4	16		
	[H]	(2, 2)	4	34	44	38	0	12	4	16		
	[H]	(2, 2)	4	35	46	38	0	12	4	16		
	[H]	(2, 2)	4	34	46	38	0	12	4	16		
	[O]	(10, 10)	20	369	1796	1463	120	552	63,504	1,048,576		
	[N]	(10, 10)	20	410	1950	1543	130	590	63,504	1,048,576		
<i>C₂H₃NO</i>	[C]	(10, 10)	20	591	1929	1597	126	604	63,504	1,048,576	130	4
	[C]	(10, 10)	20	396	1871	1503	125	578	63,504	1,048,576		
	[H]	(2, 2)	4	35	46	38	0	12	4	16		
	[H]	(2, 2)	4	35	46	38	0	12	4	16		
	[H]	(2, 2)	4	34	43	38	0	12	4	16		
	[N]	(10, 10)	20	371	1901	1532	104	568	63,504	1,048,576		
	[O]	(10, 10)	20	383	1868	1544	116	572	63,504	1,048,576		
<i>C₂H₅NO</i>	[C]	(10, 10)	20	361	1927	1589	107	580	63,504	1,048,576	165	4
	[C]	(10, 10)	20	343	1813	1432	134	568	63,504	1,048,576		
	[H]	(2, 2)	4	35	47	38	0	12	4	16		
	[H]	(2, 2)	4	35	47	38	0	12	4	16		
	[H]	(2, 2)	4	35	46	38	0	12	4	16		
	[H]	(2, 2)	4	35	48	38	0	12	4	16		
	[H]	(2, 2)	4	35	48	38	0	12	4	16		
	[N]	(10, 10)	20	375	1906	1545	94	568	63,504	1,048,576		
	[O]	(10, 10)	20	635	1865	1424	139	572	63,504	1,048,576		
<i>CH₄N₂O</i>	[C]	(10, 10)	20	633	1809	1405	142	568	63,504	1,048,576	119	4
	[N]	(10, 10)	20	655	1877	1389	131	588	63,504	1,048,576		
	[H]	(2, 2)	4	34	43	38	0	12	4	16		
	[H]	(2, 2)	4	35	47	38	0	12	4	16		
	[H]	(2, 2)	4	34	44	38	0	12	4	16		
	[H]	(2, 2)	4	33	42	38	0	12	4	16		
	[N]	(10, 10)	20	408	1925	1500	117	578	63,504	1,048,576		
	[O]	(10, 10)	20	444	1811	1437	122	564	63,504	1,048,576		
<i>NOCl</i>	[N]	(8, 10)	16	223	897	628	88	300	3,136	65,536	62	4
	[O]	(8, 10)	16	219	891	636	80	300	3,136	65,536		
	[Cl]	(12, 18)	24	342	2441	2117	109	738	48,400	16,777,216		
<i>HOSCN</i>	[H]	(2, 2)	4	34	43	38	0	12	4	16	98	4
	[O]	(10, 10)	20	454	1838	1427	199	619	63,504	1,048,576		
	[S]	(15, 18)	30	1,081	4384	4018	205	1351	25,050,025	1,073,741,824		
	[C]	(10, 10)	20	651	1911	1534	146	600	63,504	1,048,576		
	[N]	(10, 10)	20	558	2021	1622	143	646	63,504	1,048,576		

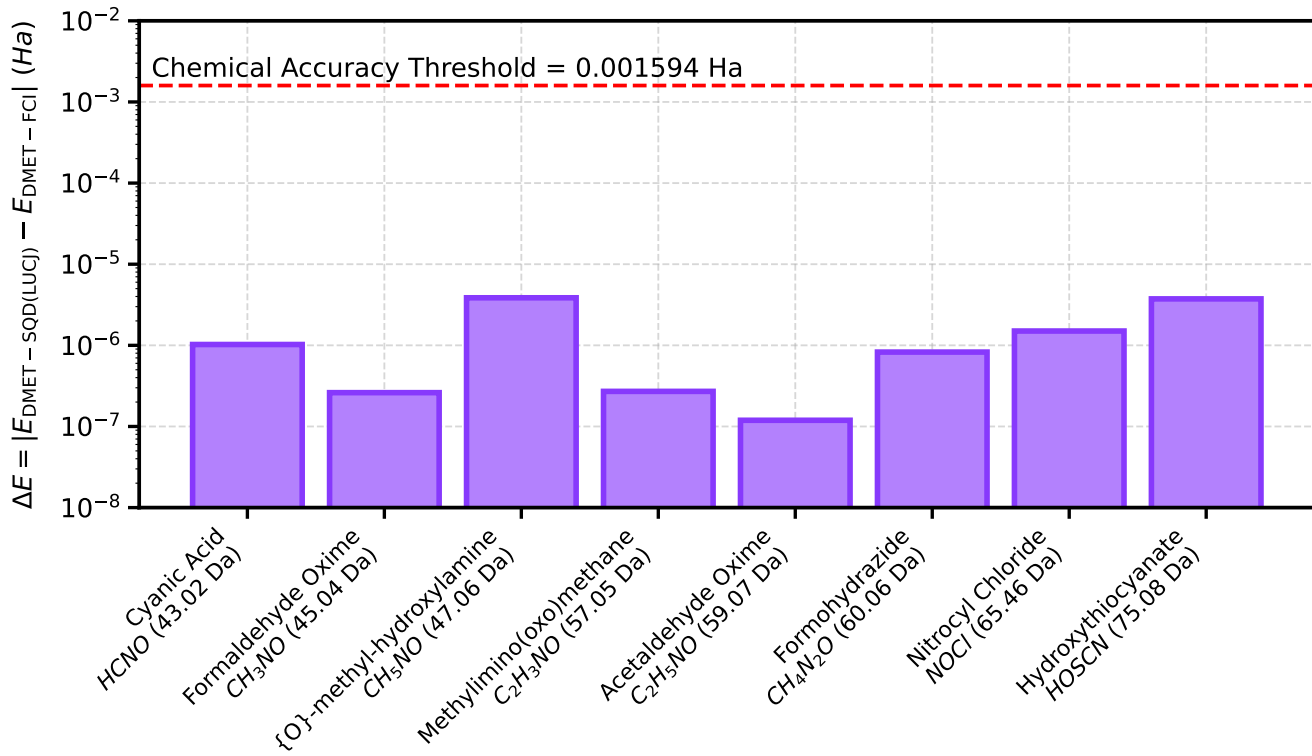


Figure 4.1. Comparison of the DMET-SQD energies obtained for the set of studied molecules on IBM Sherbrooke Quantum Hardware (4th – 5th June, 2025) with DMET-FCI. All the energies obtained are within the chemical accuracy criterion (1 kcal/mol \approx 0.001594 Ha), which is marked with the red-dashed line. The x-axis denotes the name of the studied molecule, the molecular formula and the molecular weight. The y-axis denotes the absolute energy difference between the energy obtained through quantum hardware using DMET-SQD ($E_{DMET-SQD}$) and the reference energy $E_{DMET-FCI}$, which is defined as ΔE .

with all systems achieving energy deviations below 10^{-5} Ha and electron number errors below 10^{-7} by $N_{ii} = 4$. Notably, this convergence behavior is consistent across molecules with varying chemical composition and molecular weight, indicating that the DMET-SQD workflow is robust with respect to system size within the studied regime. These results demonstrate that, despite aggressive fragmentation (one-atom-per-fragment) and minimal basis sets, DMET-SQD is able to recover correlation energies consistent with the reference DMET-FCI solver to within chemical accuracy.

Moreover, SQD's reliance on recovering signal from noisy configurations, evidenced by the need for only 2% meaningful signal amid raw noisy data in benchmark cases²⁸, reveals a deep hardware dependence that, while enabling NISQ-scale simulations, introduces inefficiencies tied to noise levels. In lower-noise regimes (higher signal configurations), the subspace dimension d could remain fixed, but fewer invalid configurations would require correction via the iterative orbital occupancy updates, potentially shifting the burden to the quantum sampler itself. Sampling from this single ansatz distribution, however, introduces key caveats³¹: notably, the risk of repetitive over-sampling of dominant configurations, leaving scant opportunity to capture rarer determinants that contribute non-negligibly to the true ground state.

Although lower hardware noise increases the fidelity of sampled configurations, it simultaneously suppresses the population of symmetry-breaking configurations. Configuration Recovery relies upon these noisy configurations to expand the sampled subspace using the orbital-occupancy distribution as a reference. In the extreme low-noise limit, this reduced exploration can narrow the recoverable determinant space and ultimately degrade the accuracy of SQD. Modern trapped-ion platforms achieve two-qubit gate fidelities of $\approx 99.92\%$ (Quantinuum)⁹⁴, $\approx 99.99\%$ (IONQ)⁹⁵, neutral-atom arrays report two-qubit fidelities approaching 99.5% (QuEra)⁹⁶, and superconducting qubits have recently achieved $\approx 99.5\%$ (Rigetti)⁹⁷, $\approx 99.88\%$ (IBM)⁹⁸, $\approx 99.93\%$ (IQM)⁹⁹ two-qubit fidelities, all of which influence the balance between valid and recoverable configurations in SQD. In ultra-low-noise regimes, the sampling distribution would collapse onto a few high-weight determinants, limiting subspace diversity, whereas moderate noise will increase the off-symmetry samples needed for SQD to reconstruct correlation-relevant determinants.

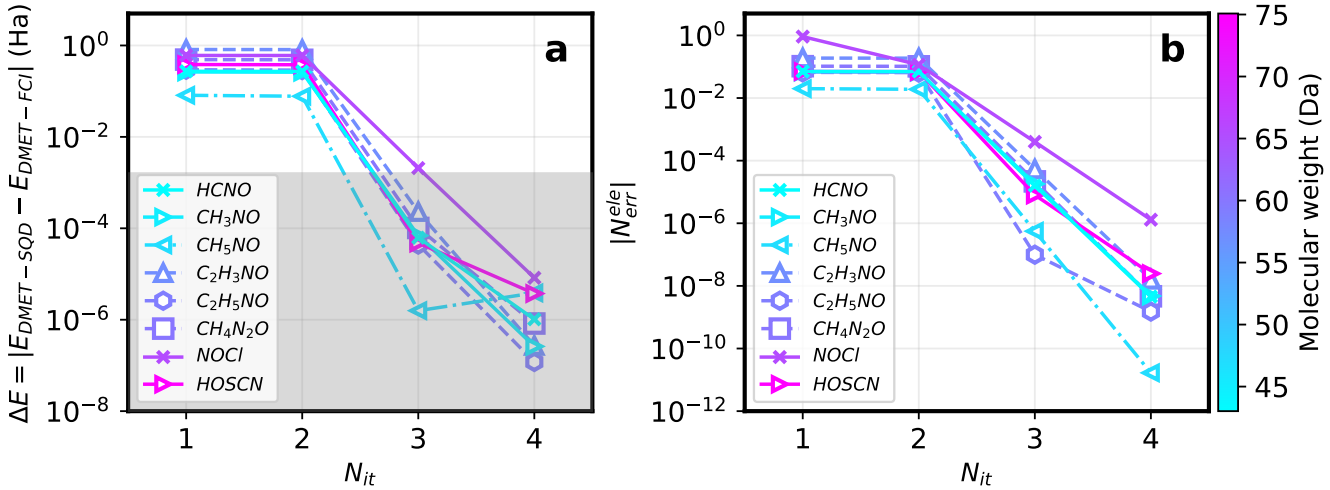


Figure 4.2. Convergence behavior of the DMET-SQD energies for a set of molecular systems. (a) Absolute energy deviation with respect to the final energy obtained through DMET-FCI, $\Delta E = |E_{\text{DMET-SQD}} - E_{\text{DMET-FCI}}|$ (Ha), (b) Corresponding absolute electron-number error, $|N_{\text{err}}^{\text{ele}}| = |\sum_y^{N_{\text{frag}}} N_y^{\text{ele}} - N_{\text{true}}|$ as given in Eq. (13), as a function of the iteration number N_{it} . Different molecular systems are distinguished by marker style, while the color scale denotes molecular weight.

5 Conclusion

In this work, we have successfully performed quantum simulation of a set of natural ligand-like molecules in the STO-3G basis set (whose molecular weights are between 40 Da and 76 Da). We employed DMET as a classical fragmentation technique followed by SQD as a high-level solver. The simulations were run on IBM’s Eagle R3 (IBM Sherbrooke) superconducting quantum computing hardware. All the results obtained were benchmarked against DMET-FCI and were found to be within chemical accuracy.

Thereby, the current NISQ hardware seems to show potential to perform quantum sampling experiments, leading to classical sub-space diagonalization in post-processing with high accuracy. This paves the way for potential industrial use-cases in the field of quantum computer-aided drug design and materials design.

That being said, although SQD ensures that the noisy configurations are recovered into the symmetry space by using the average orbital occupancy distributions as reference, this does not guarantee that the noisy configurations are stochastically converted into determinants with a non-negligible contribution to the true ground state. The procedure still might lead to obtaining configurations from the symmetry space, which contribute little to the final energy estimate.

This highlights the need for approaches that explicitly promote compactness in the selected subspace, where the retained configurations are guided by user-defined criteria rather than by sampling alone. By constraining the search to a compact and size-controlled subspace, one can more reliably concentrate quantum and classical resources only on the determinants most relevant to the target state, leading to an overall reduction of computational cost for the procedure.

Acknowledgements

The authors acknowledge the use of IBM Quantum services for this work. The authors would also like to extend appreciation to the advisors of Qclairvoyance Quantum Labs for their support, constructive discussions, and inspiration throughout the preparation of this work.

Funding

This research received no specific grant from any funding agency in the public, commercial, or not-for-profit sectors.

Competing interests

R.M. and R.V. are paid consultants at Qclairvoyance Quantum Labs. The other authors declare no competing interests.

References

- Levine, I. N. *Molecular Orbital Theory*, chap. 16, 653–710 (Pearson Education, Boston, 2014), 7 edn.
- Shayit, A. *et al.* Numerically exact configuration interaction at quadrillion-determinant scale. *Nat. Commun.* **16**, 11016 (2025), DOI: [10.1038/s41467-025-65967-7](https://doi.org/10.1038/s41467-025-65967-7).
- Franzke, Y. J., Treß, R., Pazdera, T. M. & Weigend, F. Error-consistent segmented contracted all-electron relativistic basis sets of double- and triple-zeta quality for nmr shielding constants. *Phys. Chem. Chem. Phys.* **21**, 16658–16664 (2019), DOI: [10.1039/C9CP02382H](https://doi.org/10.1039/C9CP02382H).
- Gao, H., Imamura, S., Kasagi, A. & Yoshida, E. Distributed implementation of full configuration interaction for one trillion determinants. *J. Chem. Theory Comput.* **20**, 1185–1192 (2024), DOI: [10.1021/acs.jctc.3c01190](https://doi.org/10.1021/acs.jctc.3c01190).
- Hehre, W. J., Stewart, R. F. & Pople, J. A. Self-consistent molecular-orbital methods. i. use of gaussian expansions of slater-type atomic orbitals. *The J. Chem. Phys.* **51**, 2657–2664 (1969), DOI: [10.1063/1.1672392](https://doi.org/10.1063/1.1672392).
- Fock, V. Näherungsmethode zur lösung des quantenmechanischen mehrkörperproblems. *Zeitschrift für Physik* **61**, 126–148 (1930), DOI: [10.1007/BF01340294](https://doi.org/10.1007/BF01340294).
- Kirssopp, J. J. M. *et al.* Quantum computational quantification of protein–ligand interactions. *Int. J. Quantum Chem.* **122**, e26975 (2022), DOI: [10.1002/qua.26975](https://doi.org/10.1002/qua.26975).
- Malone, F. D. *et al.* Towards the simulation of large scale protein–ligand interactions on nisq-era quantum computers. *Chem. Sci.* **13**, 3094–3108 (2022), DOI: [10.1039/D1SC05691C](https://doi.org/10.1039/D1SC05691C).
- Bowling, P. E., Broderick, D. R. & Herbert, J. M. Convergent protocols for computing protein–ligand interaction energies using fragment-based quantum chemistry. *J. Chem. Theory Comput.* **21**, 951–966 (2025), DOI: [10.1021/acs.jctc.4c01429](https://doi.org/10.1021/acs.jctc.4c01429).
- Barton, D. H. R. & Cookson, R. C. The principles of conformational analysis. *Q. Rev. Chem. Soc.* **10**, 44–82 (1956), DOI: [10.1039/QR9561000044](https://doi.org/10.1039/QR9561000044).
- Mancini, G., Fusè, M., Lazzari, F. & Barone, V. Fast exploration of potential energy surfaces with a joint venture of quantum chemistry, evolutionary algorithms and unsupervised learning. *Digit. Discov.* **1**, 790–805 (2022), DOI: [10.1039/D2DD00070A](https://doi.org/10.1039/D2DD00070A).
- Anurag, K. S. V. *et al.* Potential energy surface scan of *n*-butane using various quantum chemistry software. *Authorea* (2025), DOI: [10.22541/au.174624847.78353339/v2](https://doi.org/10.22541/au.174624847.78353339/v2).
- Hao, Y., Ding, Q., Wang, X. & Yuan, X. Large-scale efficient molecule geometry optimization with hybrid quantum-classical computing. *arXiv* (2025), DOI: [10.48550/arXiv.2509.07460](https://doi.org/10.48550/arXiv.2509.07460).
- Shajan, A. *et al.* Toward quantum-centric simulations of extended molecules: Sample-based quantum diagonalization enhanced with density matrix embedding theory. *J. Chem. Theory Comput.* **21**, 6801–6810 (2025), DOI: [10.1021/acs.jctc.5c00114](https://doi.org/10.1021/acs.jctc.5c00114).
- Kawashima, Y. *et al.* Optimizing electronic structure simulations on a trapped-ion quantum computer using problem decomposition. *Commun. Phys.* **4**, 245 (2021), DOI: [10.1038/s42005-021-00751-9](https://doi.org/10.1038/s42005-021-00751-9).
- O’Malley, P. J. J. *et al.* Scalable quantum simulation of molecular energies. *Phys. Rev. X* **6**, 031007 (2016), DOI: [10.1103/PhysRevX.6.031007](https://doi.org/10.1103/PhysRevX.6.031007).
- Schuch, N. & Verstraete, F. Computational complexity of interacting electrons and fundamental limitations of density functional theory. *Nat. Phys.* **5**, 732–735 (2009), DOI: [10.1038/nphys1370](https://doi.org/10.1038/nphys1370).
- Cao, Y. *et al.* Quantum chemistry in the age of quantum computing. *Chem. Rev.* **119**, 10856–10915 (2019), DOI: [10.1021/acs.chemrev.8b00803](https://doi.org/10.1021/acs.chemrev.8b00803).
- Aspuru-Guzik, A., Dutoi, A. D., Love, P. J. & Head-Gordon, M. Simulated quantum computation of molecular energies. *Science* **309**, 1704–1707 (2005), DOI: [10.1126/science.1113479](https://doi.org/10.1126/science.1113479).
- Eisert, J. & Preskill, J. Mind the gaps: The fraught road to quantum advantage. *arXiv* **arXiv:2510.19928** (2025), DOI: [10.48550/arXiv.2510.19928](https://doi.org/10.48550/arXiv.2510.19928).
- Kitaev, A. Y. Quantum measurements and the abelian stabilizer problem. *arXiv:quant-ph/9511026* (1995).
- Gilyén, A., Su, Y., Low, G. H. & Wiebe, N. Quantum singular value transformation and beyond: Exponential improvements for quantum matrix arithmetics. In *Proceedings of the 51st Annual ACM SIGACT Symposium on Theory of Computing*, STOC ’19, 193–204, DOI: [10.1145/3313276.3316366](https://doi.org/10.1145/3313276.3316366).
- Wang, X. *et al.* Randomized quantum singular value transformation. *arXiv* (2025), DOI: [10.48550/arXiv.2510.06851](https://doi.org/10.48550/arXiv.2510.06851).

24. Preskill, J. Quantum computing in the nisq era and beyond. *Quantum* **2**, 79 (2018), DOI: [10.22331/q-2018-08-06-79](https://doi.org/10.22331/q-2018-08-06-79).
25. Peruzzo, A. *et al.* A variational eigenvalue solver on a photonic quantum processor. *Nat. Commun.* **5**, 4213 (2014), DOI: [10.1038/ncomms5213](https://doi.org/10.1038/ncomms5213).
26. Belaloui, N. E. *et al.* Ground-state energy estimation on current quantum hardware through the variational quantum eigensolver: A practical study. *J. Chem. Theory Comput.* **21**, 6777–6792 (2025), DOI: [10.1021/acs.jctc.4c01657](https://doi.org/10.1021/acs.jctc.4c01657).
27. Tilly, J. *et al.* The variational quantum eigensolver: A review of methods and best practices. *Phys. Reports* **986**, 1–128 (2022), DOI: [10.1016/j.physrep.2022.08.003](https://doi.org/10.1016/j.physrep.2022.08.003).
28. Robledo-Moreno, J. *et al.* Chemistry beyond the scale of exact diagonalization on a quantum-centric supercomputer. *Sci. Adv.* **11**, eadu9991 (2025), DOI: [10.1126/sciadv.adu9991](https://doi.org/10.1126/sciadv.adu9991).
29. Kanno, K. *et al.* Quantum-selected configuration interaction: Classical diagonalization of hamiltonians in subspaces selected by quantum computers. *arXiv* (2023), DOI: [10.48550/arXiv.2302.11320](https://doi.org/10.48550/arXiv.2302.11320).
30. Evangelista, F. A. Adaptive multiconfigurational wave functions. *The J. Chem. Phys.* **140**, 124114 (2014), DOI: [10.1063/1.4869192](https://doi.org/10.1063/1.4869192).
31. Reinholdt, P. *et al.* Critical limitations in quantum-selected configuration interaction methods. *J. Chem. Theory Comput.* **21**, 6811–6822 (2025), DOI: [10.1021/acs.jctc.5c00375](https://doi.org/10.1021/acs.jctc.5c00375).
32. Alexeev, Y. *et al.* Quantum-centric supercomputing for materials science: A perspective on challenges and future directions. *Futur. Gener. Comput. Syst.* **160**, 666–710 (2024), DOI: [10.1016/j.future.2024.04.060](https://doi.org/10.1016/j.future.2024.04.060).
33. Barison, S., Robledo Moreno, J. & Motta, M. Quantum-centric computation of molecular excited states with extended sample-based quantum diagonalization. *Quantum Sci. Technol.* **10**, 025034 (2025), DOI: [10.1088/2058-9565/adb781](https://doi.org/10.1088/2058-9565/adb781).
34. Yoshioka, N. *et al.* Krylov diagonalization of large many-body hamiltonians on a quantum processor. *Nat. Commun.* **16**, 5014 (2025), DOI: [10.1038/s41467-025-59716-z](https://doi.org/10.1038/s41467-025-59716-z).
35. Campbell, E. Random compiler for fast hamiltonian simulation. *Phys. Rev. Lett.* **123**, 070503 (2019), DOI: [10.1103/PhysRevLett.123.070503](https://doi.org/10.1103/PhysRevLett.123.070503).
36. Yu, J. *et al.* Quantum-centric algorithm for sample-based krylov diagonalization. *arXiv* (2025), DOI: [10.48550/arXiv.2501.09702](https://doi.org/10.48550/arXiv.2501.09702).
37. Asthana, A. Quantum krylov algorithm using unitary decomposition for exact eigenstates of fermionic systems using quantum computers. *arXiv* (2025), DOI: [10.48550/arXiv.2512.11788](https://doi.org/10.48550/arXiv.2512.11788).
38. Piccinelli, S. *et al.* Quantum chemistry with provable convergence via randomized sample-based quantum diagonalization. *arXiv* (2025), DOI: [10.48550/arXiv.2508.02578](https://doi.org/10.48550/arXiv.2508.02578).
39. Pellow-Jarman, A. *et al.* Hivqe: Handover iterative variational quantum eigensolver for efficient quantum chemistry calculations. *arXiv* (2025), DOI: [10.48550/arXiv.2503.06292](https://doi.org/10.48550/arXiv.2503.06292).
40. Yoo, P. *et al.* Extending the handover-iterative vqe to challenging strongly correlated systems: n_2 and fe-s cluster. *arXiv* (2026), DOI: [10.48550/arXiv.2601.06935](https://doi.org/10.48550/arXiv.2601.06935).
41. Wouters, S., Jiménez-Hoyos, C. A., Sun, Q. & Chan, G. K.-L. A practical guide to density matrix embedding theory in quantum chemistry. *J. Chem. Theory Comput.* **12**, 2706–2719 (2016), DOI: [10.1021/acs.jctc.6b00316](https://doi.org/10.1021/acs.jctc.6b00316).
42. Knizia, G. & Chan, G. K.-L. Density matrix embedding: A simple alternative to dynamical mean-field theory. *Phys. Rev. Lett.* **109**, 186404 (2012), DOI: [10.1103/PhysRevLett.109.186404](https://doi.org/10.1103/PhysRevLett.109.186404).
43. Negre, A. *et al.* New perspectives on density-matrix embedding theory. *arXiv* (2025), DOI: [10.48550/arXiv.2503.09881](https://doi.org/10.48550/arXiv.2503.09881).
44. Cancès, E., Faulstich, F. M., Kirsch, A., Letourneau, E. & Levitt, A. Analysis of density matrix embedding theory around the non-interacting limit. *Commun. on Pure Appl. Math.* **78**, 1359–1410 (2025), DOI: <https://doi.org/10.1002/cpa.22244>.
45. Pham, H. Q., Bernales, V. & Gagliardi, L. Can density matrix embedding theory with the complete active space self-consistent field solver describe single and double bond breaking in molecular systems? *J. Chem. Theory Comput.* **14**, 1960–1968 (2018), DOI: [10.1021/acs.jctc.7b01248](https://doi.org/10.1021/acs.jctc.7b01248).
46. Verma, S., Hermes, M. R. & Gagliardi, L. Density matrix embedding pair-density functional theory for molecules. *The J. Phys. Chem. Lett.* **16**, 5348–5357 (2025), DOI: [10.1021/acs.jpclett.5c00829](https://doi.org/10.1021/acs.jpclett.5c00829).
47. Nakai, H. *et al.* Divide-and-conquer linear-scaling quantum chemical computations. *The J. Phys. Chem. A* **127**, 589–618 (2023), DOI: [10.1021/acs.jpca.2c06965](https://doi.org/10.1021/acs.jpca.2c06965).

48. Araujo, I. F., Park, D. K., Petruccione, F. & da Silva, A. J. A divide-and-conquer algorithm for quantum state preparation. *Sci. Reports* **11**, 6329 (2021), DOI: [10.1038/s41598-021-85474-1](https://doi.org/10.1038/s41598-021-85474-1).

49. Fedorov, D. G., Nagata, T. & Kitaura, K. Exploring chemistry with the fragment molecular orbital method. *Phys. Chem. Chem. Phys.* **14**, 7562–7577 (2012), DOI: [10.1039/C2CP23784A](https://doi.org/10.1039/C2CP23784A).

50. Yamazaki, T., Matsuura, S., Narimani, A., Saidmuradov, A. & Zaribafyan, A. Towards the practical application of near-term quantum computers in quantum chemistry simulations: A problem decomposition approach. *arXiv* (2018), DOI: [10.48550/arXiv.1806.01305](https://doi.org/10.48550/arXiv.1806.01305).

51. Bauman, N. P. & Kowalski, K. Coupled cluster downfolding methods: The effect of double commutator terms on the accuracy of ground-state energies. *The J. Chem. Phys.* **156**, 094106 (2022), DOI: [10.1063/5.0076260](https://doi.org/10.1063/5.0076260).

52. Bauman, N. P. *et al.* Coupled cluster downfolding theory in simulations of chemical systems on quantum hardware. *arXiv* (2025), DOI: [10.48550/arXiv.2507.01199](https://doi.org/10.48550/arXiv.2507.01199).

53. Hermes, M. R., Pandharkar, R. & Gagliardi, L. Variational localized active space self-consistent field method. *J. Chem. Theory Comput.* **16**, 4923–4937 (2020), DOI: [10.1021/acs.jctc.0c00222](https://doi.org/10.1021/acs.jctc.0c00222).

54. Otten, M. *et al.* Localized quantum chemistry on quantum computers. *J. Chem. Theory Comput.* **18**, 7205–7217 (2022), DOI: [10.1021/acs.jctc.2c00388](https://doi.org/10.1021/acs.jctc.2c00388).

55. Nusspickel, M. & Booth, G. H. Systematic improvability in quantum embedding for real materials. *Phys. Rev. X* **12**, 011046 (2022), DOI: [10.1103/PhysRevX.12.011046](https://doi.org/10.1103/PhysRevX.12.011046).

56. Ma, H. *et al.* Multiscale quantum algorithms for quantum chemistry. *Chem. Sci.* **14**, 3190–3205 (2023), DOI: [10.1039/D2SC06875C](https://doi.org/10.1039/D2SC06875C).

57. Xu, E., Shimamoto, Y., Ten-no, S. L. & Tsuchimochi, T. Many-body-expansion based on variational quantum eigensolver and deflation for dynamical correlation. *The J. Phys. Chem. A* **128**, 2507–2521 (2024), DOI: [10.1021/acs.jpca.4c00351](https://doi.org/10.1021/acs.jpca.4c00351).

58. Kowalski, K. & Bauman, N. P. Resource-adaptive quantum flow algorithms for quantum simulations of many-body systems: sub-flow embedding procedures. *arXiv* (2024), DOI: [10.48550/arXiv.2410.11992](https://doi.org/10.48550/arXiv.2410.11992).

59. Georges, A., Kotliar, G., Krauth, W. & Rozenberg, M. J. Dynamical mean-field theory of strongly correlated fermion systems and the limit of infinite dimensions. *Rev. Mod. Phys.* **68**, 13–125 (1996), DOI: [10.1103/RevModPhys.68.13](https://doi.org/10.1103/RevModPhys.68.13).

60. Blumenthal, E. Building intuition for dynamical mean-field theory: A simple model and the cavity method. *arXiv* (2025), DOI: [10.48550/arXiv.2507.16654](https://doi.org/10.48550/arXiv.2507.16654).

61. Liu, Y. *et al.* Bootstrap embedding on a quantum computer. *J. Chem. Theory Comput.* **19**, 2230–2247 (2023), DOI: [10.1021/acs.jctc.3c00012](https://doi.org/10.1021/acs.jctc.3c00012).

62. Ballance, C. J., Harty, T. P., Linke, N. M., Sepiol, M. A. & Lucas, D. M. High-fidelity quantum logic gates using trapped-ion hyperfine qubits. *Phys. Rev. Lett.* **117**, 060504 (2016), DOI: [10.1103/PhysRevLett.117.060504](https://doi.org/10.1103/PhysRevLett.117.060504).

63. Shajan, A. *et al.* Molecular quantum computations on a protein. *arXiv* (2026), DOI: [10.48550/arXiv.2512.17130](https://doi.org/10.48550/arXiv.2512.17130).

64. Fujii, K. *et al.* Deep variational quantum eigensolver: A divide-and-conquer method for solving a larger problem with smaller size quantum computers. *PRX Quantum* **3**, 010346 (2022), DOI: [10.1103/PRXQuantum.3.010346](https://doi.org/10.1103/PRXQuantum.3.010346).

65. Lim, H. *et al.* Fragment molecular orbital-based variational quantum eigensolver for quantum chemistry in the age of quantum computing. *Sci. Reports* **14**, 2422 (2024), DOI: [10.1038/s41598-024-52926-3](https://doi.org/10.1038/s41598-024-52926-3).

66. Patra, C. *et al.* Physics-informed generative machine learning for accelerated quantum-centric supercomputing. *arXiv* (2026), DOI: [10.48550/arXiv.2512.06858](https://doi.org/10.48550/arXiv.2512.06858).

67. Bierman, J. & Liu, Y. Towards utility-scale electronic structure with sample-based quantum bootstrap embedding. *Digit. Discov.* – (2026), DOI: [10.1039/D5DD00416K](https://doi.org/10.1039/D5DD00416K).

68. Caimi, P. F. *et al.* Phase i clinical trial of the base excision repair inhibitor methoxyamine in combination with fludarabine for patients with advanced hematologic malignancies. *Oncotarget* **8**, 79864–79875 (2017), DOI: [10.18632/oncotarget.20094](https://doi.org/10.18632/oncotarget.20094).

69. Eads, J. R. *et al.* Phase i clinical trial of temozolomide and methoxyamine (trc-102), an inhibitor of base excision repair, in patients with advanced solid tumors. *Investig. New Drugs* **39**, 142–151 (2021), DOI: [10.1007/s10637-020-00962-x](https://doi.org/10.1007/s10637-020-00962-x).

70. Ghosh, A. K. & Brindisi, M. Urea derivatives in modern drug discovery and medicinal chemistry. *J. Medicinal Chem.* **63**, 2751–2788 (2020), DOI: [10.1021/acs.jmedchem.9b01541](https://doi.org/10.1021/acs.jmedchem.9b01541).

71. Listro, R. *et al.* Urea-based anticancer agents: Exploring 100 years of research with an eye to the future. *Front. Chem.* **10** (2022), DOI: [10.3389/fchem.2022.995351](https://doi.org/10.3389/fchem.2022.995351).

72. Born, M. & Oppenheimer, R. Zur Quantentheorie der Moleküle. *Annalen der Physik* **389**, 457–484 (1927), DOI: [10.1002/andp.19273892002](https://doi.org/10.1002/andp.19273892002).

73. Szabo, A. & Ostlund, N. S. *Modern Quantum Chemistry: Introduction to Advanced Electronic Structure Theory*. Dover Books on Chemistry (Dover Publications, 1996). See Section 2.4.1, pp. 89–95.

74. Jordan, P. & Wigner, E. Über das paulische äquivalenzverbot. *Zeitschrift für Physik* **47**, 631–651 (1928), DOI: [10.1007/BF01331938](https://doi.org/10.1007/BF01331938).

75. Motta, M., Sung, K. J., Whaley, K. B., Head-Gordon, M. & Shee, J. Bridging physical intuition and hardware efficiency for correlated electronic states: the local unitary cluster jastrow ansatz for electronic structure. *Chem. Sci.* **14**, 11213–11227 (2023), DOI: [10.1039/D3SC02516K](https://doi.org/10.1039/D3SC02516K).

76. Bartlett, R. J. & Musiał, M. Coupled-cluster theory in quantum chemistry. *Rev. Mod. Phys.* **79**, 291–352 (2007), DOI: [10.1103/RevModPhys.79.291](https://doi.org/10.1103/RevModPhys.79.291).

77. Jensen, F. *Introduction to Computational Chemistry* (John Wiley & Sons, Inc., Hoboken, NJ, USA, 2006). Second Edition, see Section 4.9, pp. 169–174.

78. Matsuzawa, Y. & Kurashige, Y. Jastrow-type decomposition in quantum chemistry for low-depth quantum circuits. *J. Chem. Theory Comput.* **16**, 944–952 (2020), DOI: [10.1021/acs.jctc.9b00963](https://doi.org/10.1021/acs.jctc.9b00963).

79. AbuGhanem, M. Ibm quantum computers: Evolution, performance, and future directions. *The J. Supercomput.* **81**, 687–715 (2025), DOI: [10.1007/s11227-025-07047-7](https://doi.org/10.1007/s11227-025-07047-7).

80. Horn, R. & Johnson, C. *Matrix Analysis*, chap. 4.3, 242–248 (Cambridge University Press, 2012), 2nd edn.

81. MacDonald, J. K. L. Successive approximations by the rayleigh–ritz variation method. *Phys. Rev.* **43**, 830–833 (1933), DOI: [10.1103/PhysRev.43.830](https://doi.org/10.1103/PhysRev.43.830).

82. Davidson, E. R. The iterative calculation of a few of the lowest eigenvalues and corresponding eigenvectors of large real-symmetric matrices. *J. Comput. Phys.* **17**, 87–94 (1975), DOI: [10.1016/0021-9991\(75\)90065-0](https://doi.org/10.1016/0021-9991(75)90065-0).

83. Sun, Q. *et al.* The python-based simulations of chemistry framework (pyscf). *arXiv* (2017), DOI: [10.48550/arXiv.1701.08223](https://doi.org/10.48550/arXiv.1701.08223).

84. Papakonstantinou, J. M. & Tapia, R. A. Origin and evolution of the secant method in one dimension. *The Am. Math. Mon.* **120**, 500–518 (2013), DOI: [10.4169/amer.math.monthly.120.06.500](https://doi.org/10.4169/amer.math.monthly.120.06.500).

85. Senicourt, V. *et al.* Tangelo: An open-source python package for end-to-end chemistry workflows on quantum computers. *arXiv* (2022), DOI: [10.48550/arXiv.2206.12424](https://doi.org/10.48550/arXiv.2206.12424).

86. The ffsim developers. *ffsim: Faster simulations of fermionic quantum circuits, v0.0.56.* qiskit-community (2025). Accessed: 2025-11-11.

87. Javadi-Abhari, A. *et al.* Quantum computing with qiskit. *arXiv* (2024), DOI: [10.48550/arXiv.2405.08810](https://doi.org/10.48550/arXiv.2405.08810).

88. Virtanen, P. *et al.* SciPy 1.0: Fundamental Algorithms for Scientific Computing in Python. *Nat. Methods* **17**, 261–272 (2020), DOI: [10.1038/s41592-019-0686-2](https://doi.org/10.1038/s41592-019-0686-2).

89. Ai, Y., Sun, Q. & Jiang, H. Efficient multiconfigurational quantum chemistry approach to single-ion magnets based on density matrix embedding theory. *The J. Phys. Chem. Lett.* **13**, 10627–10634 (2022), DOI: [10.1021/acs.jpclett.2c02890](https://doi.org/10.1021/acs.jpclett.2c02890).

90. Mitra, A., Pham, H. Q., Pandharkar, R., Hermes, M. R. & Gagliardi, L. Excited states of crystalline point defects with multireference density matrix embedding theory. *The J. Phys. Chem. Lett.* **12**, 11688–11694 (2021), DOI: [10.1021/acs.jpclett.1c03229](https://doi.org/10.1021/acs.jpclett.1c03229).

91. Ai, Y., Li, Z.-W., Guan, Z.-B. & Jiang, H. Density matrix embedding theory-based multiconfigurational quantum chemistry approach to lanthanide single-ion magnets. *J. Chem. Theory Comput.* **21**, 9631–9640 (2025), DOI: [10.1021/acs.jctc.5c01336](https://doi.org/10.1021/acs.jctc.5c01336).

92. Li, G., Ding, Y. & Xie, Y. Tackling the qubit mapping problem for nisq-era quantum devices. *arXiv* (2019), DOI: [10.48550/arXiv.1809.02573](https://doi.org/10.48550/arXiv.1809.02573).

93. Landrum, G. *et al.* Rdkit: Open-source cheminformatics software(2025), DOI: [10.5281/zenodo.17232453](https://doi.org/10.5281/zenodo.17232453).

94. Ransford, A. *et al.* Helios: A 98-qubit trapped-ion quantum computer. *arXiv* (2025), DOI: [10.48550/arXiv.2511.05465](https://doi.org/10.48550/arXiv.2511.05465).

95. Hughes, A. C. *et al.* Trapped-ion two-qubit gates with >99.99% fidelity without ground-state cooling. *arXiv* (2025), DOI: [10.48550/arXiv.2510.17286](https://doi.org/10.48550/arXiv.2510.17286).
96. Evered, S. J. *et al.* High-fidelity parallel entangling gates on a neutral-atom quantum computer. *Nature* **622**, 268–272 (2023), DOI: [10.1038/s41586-023-06481-y](https://doi.org/10.1038/s41586-023-06481-y).
97. Du, Z. *et al.* Optimizing inter-chip coupler link placement for modular and chiplet quantum systems. *arXiv* (2025), DOI: [10.48550/arXiv.2509.10409](https://doi.org/10.48550/arXiv.2509.10409).
98. IBM Quantum. Ibm quantum — heron & ibm boston processor listings. https://quantum.cloud.ibm.com/computers?processorType=Heron&system=ibm_boston (2026). Accessed: 28 January 2026.
99. Marxer, F. *et al.* Above 99.9% fidelity single-qubit gates, two-qubit gates, and readout in a single superconducting quantum device. *arXiv* (2025), DOI: [10.48550/arXiv.2508.16437](https://doi.org/10.48550/arXiv.2508.16437).
100. Krantz, P. *et al.* A quantum engineer’s guide to superconducting qubits. *Appl. Phys. Rev.* **6**, 021318 (2019), DOI: [10.1063/1.5089550](https://doi.org/10.1063/1.5089550).

SUPPLEMENTARY INFORMATION

A Geometric Coordinates of the Studied Molecules

Table A.1. Geometric co-ordinates of the molecules used for simulation(geometry-optimized upto force-field level)⁹³.

Molecule	Atom	Geometric Coordinates		
		x	y	z
Cyanic Acid (<i>HOCN</i>)	H	-1.458587	-0.272810	0.065495
	O	-0.600578	0.099568	-0.321249
	C	0.544407	0.090463	0.422709
	N	1.514757	0.082779	1.053115
Formaldehyde Oxime (<i>CH₃NO</i>)	C	-0.910484	-0.020915	-0.332484
	H	2.170747	-0.116917	0.612439
	H	-1.005526	1.043453	-0.507441
	H	-1.760983	-0.667161	-0.500891
	N	0.207852	-0.523560	0.074740
	O	1.298394	0.285100	0.293422
Methoxyamine (<i>CH₅NO</i>)	C	-0.966149	0.201296	0.149956
	H	-1.000265	0.965450	-0.658496
	H	-1.667205	0.516700	0.949826
	H	-1.306933	-0.785003	-0.237043
	H	1.882536	0.441132	-0.409602
	H	1.601346	-1.163838	-0.023188
	N	1.132081	-0.281427	-0.328214
	O	0.324588	0.105691	0.692069
Methyl Isocyanate (<i>C₂H₃NO</i>)	C	-0.872655	-0.048579	-0.012732
	C	1.498758	0.200579	-0.121172
	H	-0.658520	-0.731912	0.839315
	H	-1.419752	-0.612203	-0.796487
	H	-1.514077	0.782782	0.345983
	N	0.351223	0.500017	-0.581535
	O	2.615024	-0.090684	0.326629
	C	-1.321954	0.079847	-0.059915
Acetaldehyde Oxime (<i>C₂H₅NO</i>)	C	0.125140	0.194559	0.278307
	H	-1.848828	-0.492848	0.731931
	H	-1.772167	1.091808	-0.134570
	H	-1.440397	-0.441345	-1.033016
	H	0.567039	1.175157	0.409184
	H	2.659033	0.076802	0.861245
	N	0.845312	-0.873562	0.413794
	O	2.186822	-0.810420	0.726078
Carbamide / Urea (<i>CH₄N₂O</i>)	C	0.023609	0.174787	0.475047
	H	2.152264	-0.041841	0.244225
	H	1.187776	-0.518005	-1.199231
	H	-2.122930	0.259006	0.346006
	H	-1.304030	-0.342648	-1.139910
	N	-1.243207	0.016569	-0.161562
	N	1.224229	-0.157069	-0.220304
	O	0.082288	0.609201	1.655728
Nitrosyl Chloride (<i>NOCl</i>)	N	-0.222631	0.458624	0.000000
	O	-1.157638	-0.281711	0.000000
	Cl	1.380269	-0.176914	0.000000
Hydroxythiocyanate (<i>HOSCN</i>)	H	-1.576204	0.567554	-0.304395
	O	-1.272167	0.443194	0.630206
	S	-0.421261	-1.048230	0.616500
	C	1.126988	-0.244750	0.353656
	N	2.142645	0.282231	0.181157

B Energy Results

Table B.1. Energy results obtained from the DMET-SQD simulations for the studied molecules. ΔE denotes the absolute energy difference between $E_{\text{DMET-FCI}}$ and $E_{\text{DMET-SQD}}$, i.e., $\Delta E = |E_{\text{DMET-FCI}} - E_{\text{DMET-SQD}}|$ in Hartree.

Molecule	$E_{\text{DMET-SQD}} (\text{Ha})$	$E_{\text{DMET-FCI}} (\text{Ha})$
Cyanic Acid (HOCN)	-165.80748733	-165.80748835
Formaldehyde Oxime (CH_3NO)	-166.89443901	-166.89443875
Methoxyamine (CH_5NO)	-168.04584566	-168.04584180
Methyl Isocyanate ($\text{C}_2\text{H}_3\text{NO}$)	-204.57166716	-204.57166689
Acetaldehyde Oxime ($\text{C}_2\text{H}_5\text{NO}$)	-205.56816508	-205.56816496
Carbamide / Urea ($\text{CH}_4\text{N}_2\text{O}$)	-221.44130237	-221.44130142
Nitrosyl Chloride (NOCl)	-582.38458086	-582.38458236
Hydroxythiocyanate (HOSCN)	-559.05055857	-559.05056231

C Quantum Computing Hardware Calibration Data - IBM Sherbrooke

Table C.1. Calibration metrics for the Eagle R3 processor (IBM Sherbrooke, containing 127 qubits) recorded on 4 June 2025 at 01:48:22 EST. These values correspond to the device's pre-execution calibration snapshot, including coherence times (T_1 , T_2), qubit frequency, anharmonicity, readout assignment errors, gate error rates, and gate durations¹⁰⁰.

Parameter	Value
T_1	270.447138 μs
T_2	211.026521 μs
Frequency	4.794027 GHz
Anharmonicity	-0.310939 GHz
Readout assignment error	0.021240
$P(0 1)$	0.020507
$P(1 0)$	0.019042
Readout length	1216.0 ns
Identity gate error	0.000244
R_z gate error	0.0
\sqrt{X} (S_x) gate error	0.000244
Pauli-X gate error	0.000244
ECR gate error	0.006767
Gate time	533.333333 ns